Materials and Design 197 (2021) 109246

Contents lists available at ScienceDirect

Materials and Design

journal homepage: www.elsevier.com/locate/matdes

# Simultaneous improvement of plasticity and strength of metallic glasses by tailoring residual stress: Role of stress gradient on shear banding

Lei Zhao [a], Dongxue Han [a], Shuai Guan [a], Xianzheng Lu [a], Kangcheung Chan [a,*], Gang Wang [b]

[a] Advanced Manufacturing Technology Research Centre, Department of Industrial and Systems Engineering, The Hong Kong Polytechnic University, Hung Hom, Kowloon, Hong Kong
[b] Laboratory for Microstructures, Institute of Materials, Shanghai University, Shanghai 200444, China

## HIGHLIGHTS

- Surface-imprinted metallic glasses exhibit enhanced plasticity and strength due to deformation-induced redisual stresses.
- Surface compressive residual stress promotes earlier yielding, acting as stimulators for multiple shear band initiation.
- The stress gradient raised from the residual stress slows down shear banding dynamics via deflection and branching.
- The stress gradient perturbs the autocatalytic percolation of shear transformation zones in the shear front.

## GRAPHICAL ABSTRACT

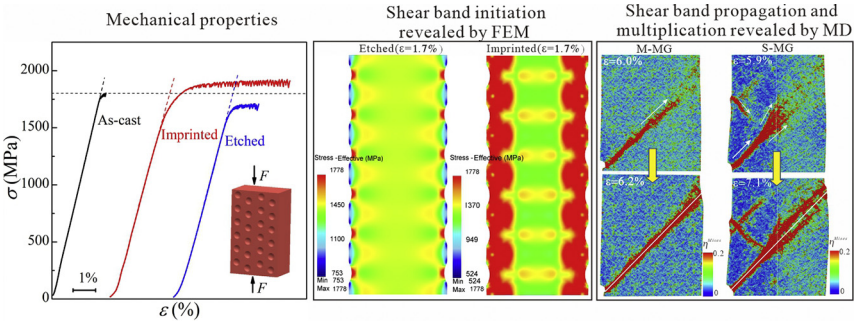


## ARTICLE INFO

*Article history:*
Received 10 August 2020
Received in revised form 30 September 2020
Accepted 18 October 2020
Available online 21 October 2020

*Keywords:*
Metallic glasses
Residual stress
Surface imprinting
Mechanical properties
Shear banding behavior

## ABSTRACT

Inducing residual stress in metallic glasses (MGs) is recognized to be beneficial for plasticity but the mechanisms on how it affects shear band nucleation, propagation and multiplication remain poorly understood. With the aid of experimental and computational approaches, we address this issue by comparatively studying the deformation behavior of two types of MG samples, which were individually prepared by surface imprinting and photo-chemical etching but having similar surface patterns. Results showed that the imprinted MGs exhibit simultaneously enhanced plasticity and compressive strength, while the etched ones show limited plasticity improvement and reduced strength. The enhanced mechanical properties of the imprinted MGs are attributed to the compressive residual stresses generated near the surfaces, rather than the resultant geometrical pits. Finite element analysis revealed that the residual stress induces obvious stress gradient and inhomogeneous plastic deformation, which facilitate heterogeneous nucleation of multiple shear bands near the surfaces. Complementary atomistic simulations further revealed that the stress gradient resulting from the residual stress slows down the shear banding dynamics and causes deflection and branching, which consequently promotes shear band multiplication during propagation. This work uncovers the interactions between the residual stresses and shear bands, which are useful for processing MGs with desirable mechanical properties.



## 1. Introduction

Due to the liquid-like atomic structures combined with strong metallic bonds, metallic glasses (MGs) exhibit a superior combination of mechanical properties including large elastic limit, high hardness and high fracture toughness [1–4]. However, a major drawback that precludes the practical applications of most MGs as load-bearing materials is the catastrophic brittle fracture with limited macroscopic plasticity at room temperature [5,6]. The severe brittleness is ascribed to the lack of strain hardening mechanisms in MGs and the resultant rapid propagation of individual highly localized shear bands soon after yielding

* Correspondence author.
*E-mail address:* kc.chan@polyu.edu.hk (K. Chan).

https://doi.org/10.1016/j.matdes.2020.109246

[5–8]. In past decades, how to enhance the plastic deformability and thus overcome the room-temperature brittleness without sacrificing the high strength has been a hot topic in the research community [9,10]. Unlike the plastic deformation of crystalline metals that relies on lattice dislocations, the plasticity of MGs at room temperature is essentially accommodated by shear bands [11]. Therefore, to disperse the plastic strain in MGs, it is crucial to facilitate the initiation of multiple shear bands upon loading. Meanwhile, the unstable and rapid propagation of the major shear bands needs to be retarded to prevent premature failure, allowing strain accumulation throughout the sample. By controlling the shear banding behavior following this approach, many successful attempts have been made to promote the plastic deformability of MGs so far. For instance, a large plastic strain can be attained in bulk MGs through various extrinsic approaches such as geometric constraining [12,13], sample size reduction [14,15] and notch installing [16,17], and through intrinsic approaches (structural modifications) such as the addition of crystalline inclusions [18,19], accumulation of free volume (i.e., rejuvenation) [20,21] and introduction of pre-existing shear banding via mechanical treatments [22,23]. The resultant multiple shear banding process in these MGs is usually manifested as serrated plastic flow behavior, which was found to be associated with the intermittent avalanches and arrests of the operating shear bands [24–26].

In the mineral glass industry, it is well established that various glasses, such as amorphous silicate glass, can be effectively toughened by residual stress engineering. The residual stress induced by the tempering treatment in glasses exhibits a parabolic distribution with the maximum compressive stress near the surfaces [27]. It was reported that the compressive stress state near the surfaces can effectively suppress cracking, thus promoting toughness and strength [28]. Inspired by the role of residual stress in silicate glasses, recently great efforts have been also expended in promoting the plastic deformability of MGs by inducing compressive residual stress at the surfaces. Since much lower residual stresses can be induced in MGs upon quenching, due to the much higher thermal conductivity of MGs, surface pre-treatment techniques, such as shot peening [29], laser shock peening [30] and surface attrition treatment [31], have been widely adopted. For instance, Zhang et al. [29] induced compressive residual stresses in Vitreloy 1 bulk MGs using shot peening and demonstrated that the plasticity and strength of the shot-peened MGs can be greatly enhanced, both in bending and uniaxial compression. The improved mechanical properties are attributed to the compressive residual stress combined with the pre-existing shear bands generated near the shot-peened surfaces. Cao et al. [32] also found that the compressive plasticity and strength of Zr-based bulk MGs can be improved by inducing surface compressive residual stress using laser shock peening. The compressive residual stress was found to be able to suppress the propagation of cracks and shear bands, resulting in the formation of a high density of shear bands near the surfaces. In fact, the presence of tensile residual stress near the surfaces of MGs also can achieve a similar effect, as recently verified by several experimental and numerical studies [33–35]. For instance, Chen et al. [34] reported that laser surface melting produces tensile residual stress on the surface layer of the treated MGs, which was found to be capable of improving the global plasticity under compression. Cheng et al. [35] further revealed that the plasticity of MGs treated by laser surface melting is tunable by tailoring the angle between the residual stress and loading direction. Generally, no matter whether the induced residual stress near the surfaces is in a tensile or compressive state, the residual stress is superimposed with the external force upon loading (compression or tension) and can lead to the formation of mechanical heterogeneities and stress gradient. The mechanical heterogeneities and stress gradient greatly affect the shear banding behavior in MGs, hindering the generation of detrimental shear bands throughout the sample [24,36]. Although great progress has been made to phenomenally explain the enhanced mechanical properties of MGs by adjusting residual stresses, comprehensive and deep understanding of the mechanisms on how the residual stress affects shear band nucleation, propagation and multiplication in MGs, and more importantly, on how shear bands interact with the resultant stress gradient, have not yet been fully elucidated so far.

To address these issues, in this study, we fabricated and compressed two types of Zr-based bulk MG specimens, which were individually prepared by surface imprinting and photo-chemical etching, but having similar surface patterns. The surface residual stresses were adjusted in the bulk MGs using a custom-built surface imprinting process since it can produce a high level of residual stresses into much greater depths (at the level of millimeters), as compared with the conventional shot peening (< 40 μm [29]) and surface attrition treatment (< 200 μm [31]). Furthermore, it avoids the formation of obvious microstructural changes such as a high density of shear bands caused by severe plastic deformation near the surfaces. Photo-chemical etching was used to reproduce the similar surface patterns of the imprinted MG specimens without induced residual stresses. Through comparatively studying the deformation behavior of these two types of MG specimens with similar surface patterns using experimental and computational approaches, the induced residual stress was found to not only facilitate the initiation of multiple shear bands at the early deformation stage but also play a vital role in suppressing the rapid propagation of the shear bands via shear band deflection and branching in the propagation stage, both of which eventually give rise to the improved plasticity and strength of the glass. Finite element method (FEM) analysis was undertaken to illuminate the mechanisms of multiple shear band initiation near the imprinted surfaces. Moreover, complementary molecular dynamics (MD) simulations were performed to provide an atomic description of the interactions of shear bands with the stress gradient raised from the residual stress. This work is intended to provide a comprehensive elucidation of the effects of residual stresses on the nucleation, propagation and multiplication of shear bands in imprinted MGs at different length scales, which deepens our understanding on the plastic deformation behavior of mechanical heterogeneous MGs.

## 2. Methodology

### 2.1. Sample preparation and mechanical characterization

$Zr_{55}Cu_{30}Al_{10}Ni_5$ (at.%) MG with good glass-forming ability but poor compressive plasticity (<1%) [37] was chosen as the material for experimentation. MG plates with dimensions of $2 \times 12 \times 70$ mm$^3$ were fabricated by the suction casting of arc-melted mixtures of pure elements (purity > 99.99%) into a water-cooled copper mould under a Ti-gettered Argon atmosphere. The as-cast MG plates were then annealed at 623 K ($T_g \approx 685$ K [38]) for 30 min in a high vacuum thermal treatment system to relieve the residual stress, if any, generated in the casting process [39]. The fully amorphous nature of the MG plates was confirmed using X-ray diffraction with Cu $K_\alpha$ radiation (Rigaku SmartLab). The MG plates were further carefully ground and polished using abrasive papers for subsequent treatments.

Residual stresses were induced in the bulk MGs by surface imprinting using two custom-built imprinters on a servo-hydraulic MTS 810 machine at room temperature. The principle of surface imprinting adopted in this study is schematically illustrated in Fig. 1(a). The imprinters were custom-built by elaborately fixing twenty-four cemented carbide balls (with a uniform diameter of 0.80 mm) on the surfaces of two steel supports in a close-packed pattern (see the imprinted samples in Fig. 1(b)). The AB-stacking pattern was selected since it has been reported to be easier to facilitate shear band multiplication, as compared to the AA-stacking pattern [40,41]. The polished MG plate (the blue block) was imprinted by different imprinting forces ($F = 0$, 10 15 20 and 25 kN) imposed on the supports along the $Z$-direction and maintained for 1 min. Spherical imprints were thus generated on the two surfaces. The imprinted MG specimens, with dimensions of $2.0 \times 3.0 \times 5.0$ mm$^3$, were further cut from the plates using electrical discharge machining.

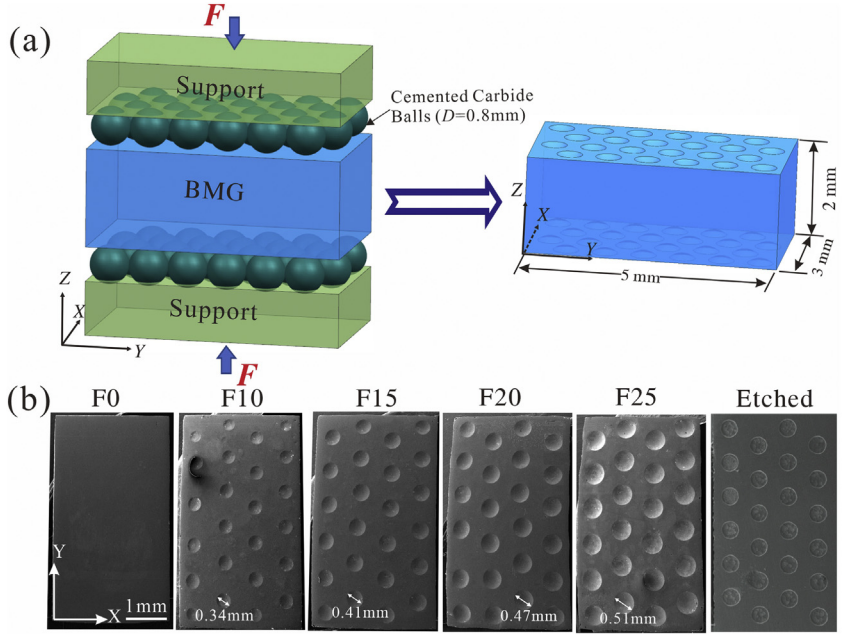


**Fig. 1.** (a) Schematic illustration of the surface imprinting approach adopted in the present study. (b) SEM images of the surface appearances of imprinted MG specimens for uniaxial compressive tests.

To clarify the effect of residual stresses induced in the imprinted MGs, specimens with the similar imprinted patterns were prepared through photo-chemical machining (PCM) for comparison. Since PCM is a chemical etching method, it can reproduce the surface patterns of imprinted MGs without inducing residual stresses. The etching patterns were designed according to the imprinted patterns. The etching depths of the patterns were controlled by the etching time. More details on the PCM process can be found in our previous publications [9,42,43]. A 3D optical profiler (ZeGage™ Pro) was used to measure the profiles of the imprinted and etched patterns.

Uniaxial compression tests were further carried out on an MTS 810 machine at room temperature. A constant strain rate of $1 \times 10^{-4}$ $s^{-1}$ was applied along the length direction (i.e., the Y-direction shown in Fig. 1(b)). Before testing, the two ends of the samples were carefully polished to ensure perpendicularity and parallelism. At least five samples were tested for each condition to ensure the reproducibility of the results. The engineering strain was measured using an extensometer, and the engineering stress was calculated using the equation $\sigma = P/A$, where $P$ is the compressive force monitored by a force cell and $A$ is the maximum cross-sectional area (i.e., $2 \times 3$ $mm^2$ in the X-Z plane) of the samples before loading. The deformation and fracture morphologies were inspected using a scanning electron microscope (SEM, Tescan VEGA3).

### 2.2. FEM simulations

FEM analysis was undertaken to investigate the formation of residual stresses in the imprinted MGs and its effect on the shear band initiation under compression. For simplicity, the actual three-dimensional deformation conditions were reduced to two-dimensional plane-strain models, both for surface imprinting and uniaxial compression (see Fig. S1 in Supplementary Materials). Meanwhile, an elastic-perfectly plastic constitutive model based on the Von Mises criterion was adapted to approximate the deformation behavior of the MGs. Although the model does not consider the effect of strain softening of MGs, the predicted variations of the stress from highly deformed areas to undeformed areas should be similar to those with the consideration of the strain softening effect. Since the stress trends are sufficient for the prediction of the potential nucleation sites of shear bands upon loading, it is justified to use the simplified model for the present numerical analysis [17]. The adopted material parameters are listed as follows: Young's modulus $E = 88$ GPa, yield stress $\sigma_y = 1778$ MPa (see the results of compression tests for the as-cast MGs) and Poisson's ratio, $\nu = 0.36$ [44]; The models were discretized with 25,000 elements using the plane-strain four-node quadrilateral element. Imprinting simulations were performed by moving the rigid imprinters to several different penetration depths obtained from the above experiments (i.e., 38 μm, 56 μm, 76 μm and 91 μm for the MGs imprinted with $F = 10$ kN, 15 kN, 20 kN and 25 kN, respectively; see the experimental results in Section 3.1). To mimic the constrained deformation of the MG specimens in the large plates, the upper and lower ends of the models (see Fig. S1(a) in Supplementary Materials) were fixed in the length direction during imprinting. After that, they were set free to allow the formation of residual stresses in the imprinted models. The obtained imprinted models were further compressed to a total strain of 2.0% in the subsequent compression simulation using a displacement-control mode.

### 2.3. MD simulations

To uncover the effect of residual stress on the shear band propagation, complementary MD simulations were conducted using LAMMPS [45] by constructing and compressing several tailored MG models without/with residual stresses. Since no appropriate interatomic potentials exist for the $Zr_{55}Cu_{30}Al_{10}Ni_5$ MG, Cu64Zr36 MG was chosen for the ease of modelling. Such a selection is acceptable since the effect of residual stress on shear banding is expected to be compositionally independent. The embedded-atom-method potential [46] was adopted to describe the atomic interactions. A monolithic MG (hereafter denoted as "M-MG"), of dimensions around $50 \times 4.8 \times 100$ $nm^3$, was fabricated through the so-called "melt-quench-duplicate-anneal" procedure [18,21]. Briefly, a small Cu64Zr36 MG cube was first prepared by quenching the melting liquid from 2000 K to 100 K. The cube was further duplicated to the dimensions of the M-MG, following by annealing at 800 K ($T_g \approx 787$ K in MD simulations) for 0.2 ns and finally cooling back to 100 K. A constant-pressure-temperature ensemble (NPT) controlled with a Nose-Hoover thermostat was adopted in the whole system [47] and periodic boundary conditions were imposed in three dimensions. Due to the as-quenched structure, the M-MG is free from residual stresses from the macroscopic point of view. To fabricate MGs

with tailored residual stresses (hereafter denoted as "S-MGs"), a procedure, referred as "elastic preload-assemble-anneal" in this study, was implemented according to the schematic diagram shown in Supplementary Fig. S2. The S-MGs were constituted using two slabs, both of which have the same width along the X-direction but different lengths along the Y-direction. Through elastically pre-straining the two slabs into the same length, residual stresses were generated within the two slabs. After assembling, the models were annealed at 750 K under a hydrostatic pressure of 1.5 GPa for 0.5 ns in order to eliminate the artificial interfaces between the slabs. Since the length (i.e., $L + \Delta L$) of slab A is a little larger than that (i.e., $L = 100$ nm) of slab B, compressive residual stress and tensile residual stress along the Y-direction was generated within the two slabs. By controlling the relative length difference (i.e., the pre-loading strain), $\Delta\varepsilon = \Delta L/(L + \Delta L)$ ($\Delta\varepsilon = 1\%$, 2% and 3%), S-MGs with different levels of residual stresses were thus tailored. The relation between $\Delta\varepsilon$ and the amplitude ($\sigma_0$) of the resultant residual stress is given in Supplementary Table S1. The atomic-scale topological structures were investigated in terms of topological short-range orders (SROs) through Voronoi analysis [48]. It should be mentioned that the S-MGs and the M-MG show the similar structures across the samples, as evidenced by the structural parameter, the fraction of the Cu-centred full icosahedron (FI) (See Supplementary Fig. S3). More details about the structural analysis are provided in the Supplementary Materials. The obtained M-MG and S-MGs were further compressed along the Y-direction at 100 K under a strain rate of $1 \times 10^8$ $s^{-1}$. The X-direction was set as a free boundary to allow for shear offset. To reduce the number of shear bands and control the shear band initiation site, a small notch was installed on the left surface, acting as a stress concentrator. The atomic-scale shear banding process was monitored by the atomic shear strain, $\eta^{Mises}$ [49] and visualized by Ovito [50]. Generally, the zones colored with large $\eta^{Mises}$ (i.e., $\eta^{Mises} > 0.2$ [18]) indicates clusters of atoms experiencing irreversible rearrangements and can be viewed as shear transformation zones (STZs), i.e., volumes of materials participated in plastic deformation under stresses [18].

## 3. Results

### 3.1. Surface observation

The MG plates were imprinted using the same indenters with different $F$ values ($F = 10$ kN, 15 kN, 20 kN and 25 kN, respectively) so as to explore the effect of $F$ on the plasticity improvement in the subsequent mechanical tests. Note that a large $F$ is expected to induce a higher level of residual stresses. Fig. 1(b) demonstrate the SEM images of the series of the imprinted MGs used for uniaxial compressive tests. It is seen from their surface appearances that the imprinted patterns were constituted with AB-stacked pits. Each pit had a constant distance of around 0.8 mm with its nearest-neighbour pit. Moreover, the pits became larger and deeper with $F$ increasing from 10 kN to 25 kN. The depths of the imprinted pits were measured to be around 38 μm, 56 μm, 76 μm and 91 μm, respectively, which correspond to 1.9% - 4.6% of the thickness of the MG samples (2.0 mm). Within the range of $F$ adopted in this study, shear bands were not visible in or around the imprinted pits (see Fig. 2). This is quite unlike the case of processing MGs using shot peening and surface attrition treatment, in which severe plastic deformation takes places and profuse shear bands can be induced near the treated surface [31,51]. However, it should be noted that when $F$ reaches 30 kN and higher values, obvious shear bands and even cracks can be observed on the imprinted surfaces, which would destroy the integrity of the materials and lead to degraded mechanical properties.

### 3.2. Mechanical properties of imprinted MGs and etched MGs

Fig. 3(a) shows the typical engineering compressive stress-strain curves of the as-cast MGs and the imprinted MGs prepared under different $F$ values. For comparison, Fig. 3(b) summarizes the variations of the measured yield strength ($\sigma_y$), ultimate strength ($\sigma_u$) and plastic strain ($\Delta\varepsilon_p$) as a function of $F$. Note that $\Delta\varepsilon_p$ is calculated by $\Delta\varepsilon_p = \varepsilon_f - \varepsilon_y$, where $\varepsilon_f$ and $\varepsilon_y$ correspond to the fracture strain ($\varepsilon_f$) and yield strain ($\varepsilon_y$), respectively, as illustrated in Fig. 3(a). The error bars were obtained through the fine-point standard deviation from the average. One can see that the as-cast MG (i.e., F0) yields at an average $\varepsilon_y$ of around 2.0% and further undergoes little plastic strain ($\Delta\varepsilon_p = 0.3\% \pm 0.1\%$) before the catastrophic fracture, analogous to what have been previously reported in the literature [37,38]. The imprinted MGs, however, yield a little earlier due to pre-existing residual stresses, since residual stresses lower the energy barrier required for irreversible shear transformation [52]. After yielding, they exhibit apparent serrations with large stress drops and hence noticeably plasticity improvement before the final failure. The serrated plastic flow is generally regarded as the characteristic signature of intermittent shear banding events, which contribute to the large plastic deformation in deformed MGs [24]. Impressively, $\Delta\varepsilon_p$ increased significantly from $0.3\% \pm 0.1\%$ to $7.1\% \pm 1.0\%$ as $F$ increased from to 0 kN to 25 kN. This was accompanied by decreasing $\sigma_y$ gradually from a value of $1778 \pm 17$ MPa to $1545 \pm 25$ MPa. Furthermore, the ultimate strength, $\sigma_u$, first increased from $1789 \pm 13$ MPa at $F = 0$ kN, reaching the maximum of $1920 \pm 21$ MPa at $F = 15$ kN, and then decreasing slightly to $1905 \pm 16$ MPa at $F = 25$ kN. It is evident that, although surface imprinting leads to reduced $\varepsilon_y$ and $\sigma_y$, it gives rise to a simultaneous improvement of $\Delta\varepsilon_p$ and $\sigma_u$, a sought-after combination of mechanical properties which are crucial for practical engineering applications of MGs.

We also prepared and compressed some etched MGs, which had a similar AB-stacking pattern with the MG imprinted with $F = 20$ kN but without reduced residual stresses, for comparison. Fig. 4(a) presents the representative profiles of the pits on the bilateral surfaces of the imprinted and etched MG. The inset of Fig. 4(a) illustrates how the profiles were obtained using the 3D optical profiler. One can see that the imprinted and etched pits almost show the same curved shape. Fig. 4(b) displays the obtained engineering stress-strain curves of the as-cast, imprinted and etched MGs. It was observed that the etched MG shows some plasticity improvement but with the average value ($1.4\% \pm 0.6\%$) much smaller than that ($7.1 \pm 1.0\%$) of the corresponding imprinted MG. Meanwhile, the resultant $\sigma_y$ ($1548 \pm 26$ MPa) and $\sigma_u$ ($1719 \pm 11$ MPa) were distinctly lower than those of the as-cast MG. Besides, Young's Modulus ($E = 75 \pm 3$ GPa) was significantly reduced as compared to those of the as-cast ($88 \pm 2$ GPa) and imprinted ($86 \pm 3$ GPa) MGs. It is obvious that the etched MGs show some improved plasticity but with greatly reduced strength. So far, the effect of geometrical defects, such as pits, holes and notches, on the mechanical behavior of MGs have been extensively investigated [16,17,41,53,54]. Such geometrical defects prepared by the removal of materials were found to induce enhanced plasticity and may even result in a phenomenon of notch strengthening [53,55]. Such a strengthening effect was not observed in the stress-strain curve of the etched MGs since the stress was calculated using the maximum cross-sectional area ($2 \times 3$ $mm^2$) rather than the minimum area. It should be noted that, when using the same method for calculating the engineering stress, similar changes in the mechanical properties (i.e., enhanced $\Delta\varepsilon_p$ and but reduced $\sigma_u$) have also been observed in MGs with pits or notches generated by the removal of materials using various approaches, such as laser surface texturing treatment [41] and electrical discharge machining [17].

### 3.3. Deformation and fracture morphologies

Fig. 5(a)–(h) display the representative lateral morphologies of the as-cast, imprinted (F10 and F20) and etched MGs obtained by SEM after the final failure. Both the side surfaces (the first column) and front surfaces (the second column) were displayed to demonstrate the shear band distributions. It can be seen that, for the as-cast MG (Fig. 5(a)–(b)), there exists one dominating primary shear band accompanied with few visible secondary shear bands on the

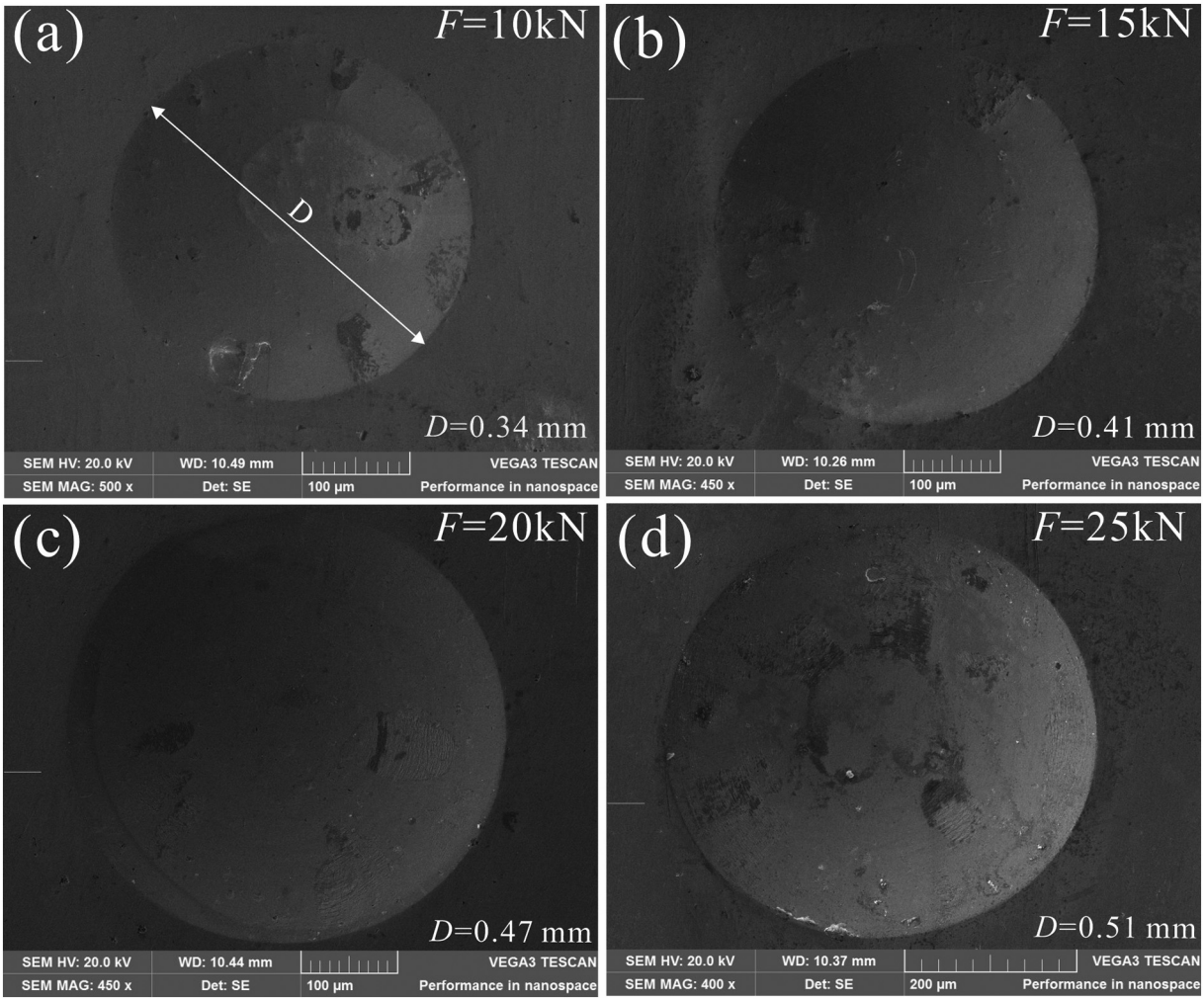


**Fig. 2.** Representative SEM images around the imprinted pits, revealing the absence of visible shear bands on the surfaces of the imprinted MGs prepared under different *F*s: (a) $F = 10$ kN; (b) $F = 15$ kN; (c) $F = 20$ kN and (d) $F = 25$ kN.

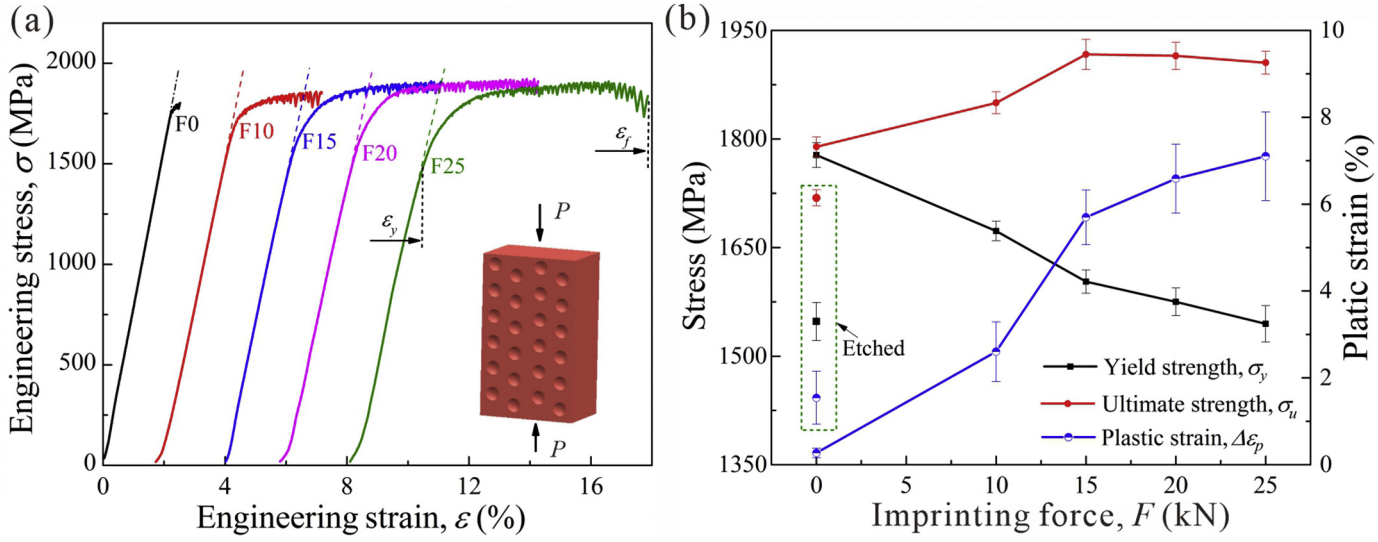


**Fig. 3.** Mechanical properties of the imprinted MGs under uniaxial compression. (a) Typical engineering stress-strain curves. $\varepsilon_y$ corresponds to the strain where the stress-strain curves deviate from the linear relationship. (b) Variations of the yield stress ($\sigma_y$), fracture stress ($\sigma_f$) and plastic strain ($\varepsilon_p$) with the imprinting force, *F*; The error bars represent the standard deviations. The data marked in the dotted box corresponds to the mechanical properties of the etched MGs extracted from Fig. 4(b).

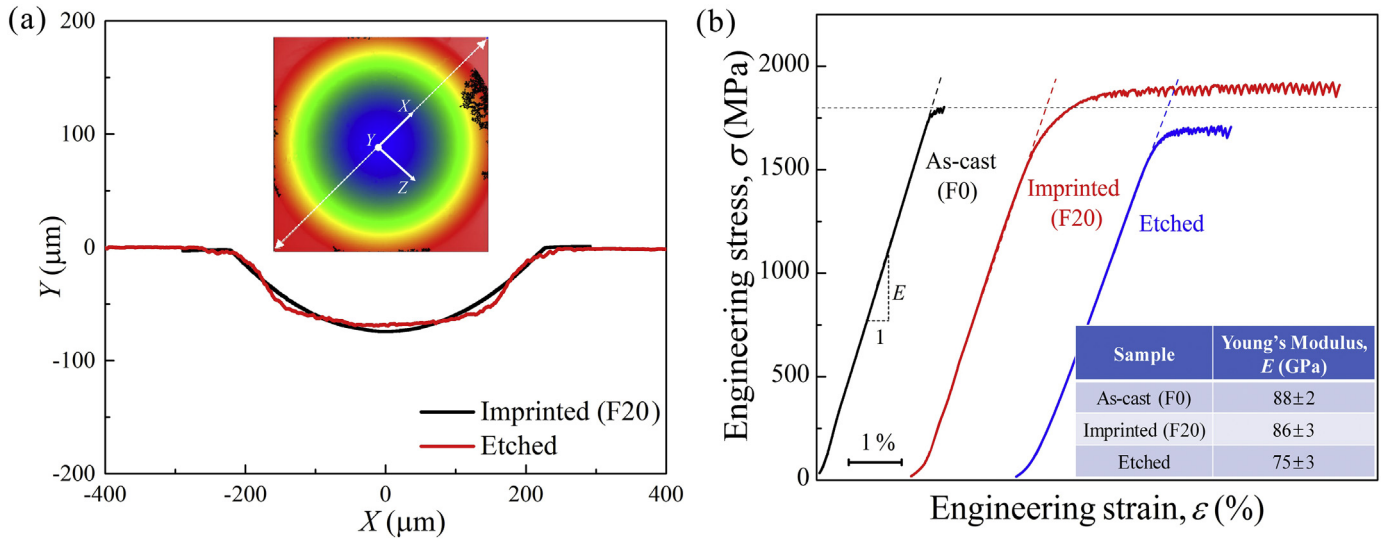


**Fig. 4.** (a) Representative profiles of the pits on the surfaces of the imprinted F20 MG and the etched MG. The inset illustrates how the profiles were measured using the 3D optical profiler. (b) Engineering stress-strain curves for the as-casted, imprinted and etched MG samples under uniaxial compression.

lateral surfaces, a typical failure mode observed in brittle MGs. The single shear band is straight throughout the sample due to strain softening after plastic deformation and the lack of microstructures that can impede its rapid propagation in the shear front [56]. In sharp contrast, the imprinted F10 and F20 MGs (Fig. 5(c)–(d) and Fig. 5(e)–(f)) demonstrate a large number of primary (denoted by the solid white arrows) and secondary (denoted by the dotted yellow arrows) shear bands on both surfaces. These profuse shear bands propagate in different directions, leading to intense intersections and interactions. Meanwhile, one can see from the side surfaces that many secondary shear bands deflect obviously from their original shear planes when they propagate in the interior of the imprinted samples. Some of the deflected shear bands even branch into tiny shear bands (marked by the box in Fig. 5(e)). The population density of the shear bands increased significantly as *F* increased from 10 kN to 20 kN. Under an *F* of 20 kN, some cracks that were derived from large shear offsets of some shear bands can be even observed at the bottom region of the pit and the middle region between the pits (marked by the dotted green arrows in Fig. 5(f)). For the etched MG (Fig. 5(g)–(h)), some primary and secondary shear bands were visible on the lateral surfaces. The population density of the shear bands was higher than that of the as-cast MG but much lower than the those of the imprinted MGs. From these SEM observations, it is clear that the shear band densities observed in the imprinted and etched MGs are in accordance with the plasticity measured from their stress-strain curves. Considering that these MGs have a similar geometry but were prepared with different pre-treatments, it can be concluded that the plasticity enhancement of the imprinted MGs should be closely associated with the capacity of shear band multiplication after surface imprinting. It should be also emphasized that the same fracture mode, i.e., shear rupture along an inclined plane, remains unchanged for the imprinted MGs, although obvious plastic deformability was achieved via the formation of multiple shear bands.

### *3.4. Correlation between residual stresses and the improved plasticity and strength*

The experimental results shown in Fig. 3 reveal that surface imprinting can greatly improve the overall mechanical properties, including the plasticity and ultimate strength, of the originally brittle MGs. This finding is very attractive considering the original brittle nature of the Zr-based MG under compression and the simplicity of the treatment. Meanwhile, within a moderate range of values of no more than 25 kN, the imprinting force, *F*, has a positive impact on the resultant plasticity and ultimate strength. It should be noted that surface imprinting not only induces obvious compressive residual stress resulting from the nonuniform plastic deformation, but also generates geometrical defects, i.e., imprinted pits, on the surfaces due to the irreversible plastic deformation [52,57]. With increasing *F*, the sizes of the imprinted pits become larger, and the resultant residual stresses near the imprinted surface are also expected to be enhanced. It has been extensively reported that both the residual stresses and geometrical defects on the sample surfaces can generate complex stress states in MGs under deformation and allow the development of a more distributed network of shear bands, thus promoting the mechanical properties of MGs [41,52,58]. To identify the involved major contributor, we, therefore, compressed several etched MGs obtained through PCM. Interestingly, the etched MG endowed with only geometrical pits exhibited a limited improvement in plasticity and, more importantly, an obvious reduction in the ultimate strength, as compared to the imprinted MGs (Fig. 4(b)). It is clear that these two types of MGs prepared with similar geometrical patterns display quite different plastic deformation behaviours, which depend on whether or not residual stresses were induced after the surface pre-treatments. The geometrical pits act as stress concentrators under deformation, which lead to the formation of multiple shear bands [41]. Nevertheless, the further induction of residual stresses via surface imprinting seems to be more effective in facilitating a high density of shear bands, as observed in Fig. 5. Through this comparison, one can infer that the improved plasticity and enhanced ultimate strength found in the imprinted MGs should mainly benefit from the residual stresses generated after surface imprinting, rather than the resultant geometrical pits.

It should be noted that mechanical pre-deformation by surface imprinting may also introduce some latent shear bands beneath the imprinted pits, although they are almost invisible from the sample surfaces under SEM observation. This phenomenon has been evidenced by Yoo and Jang who successfully observed the generation of semi-circular and radial shear bands underneath the pits in spherical indentations using the bonded interface technique [59]. The pre-existing shear bands underneath the pits may be activated to accommodate plastic strain under subsequent deformation, which is also beneficial for the global plasticity of MGs [29,60]. However, its effect should not be as prominent as the mechanically induced residual stresses in this study due to the limited volume fraction of the plastic zones beneath the pits.

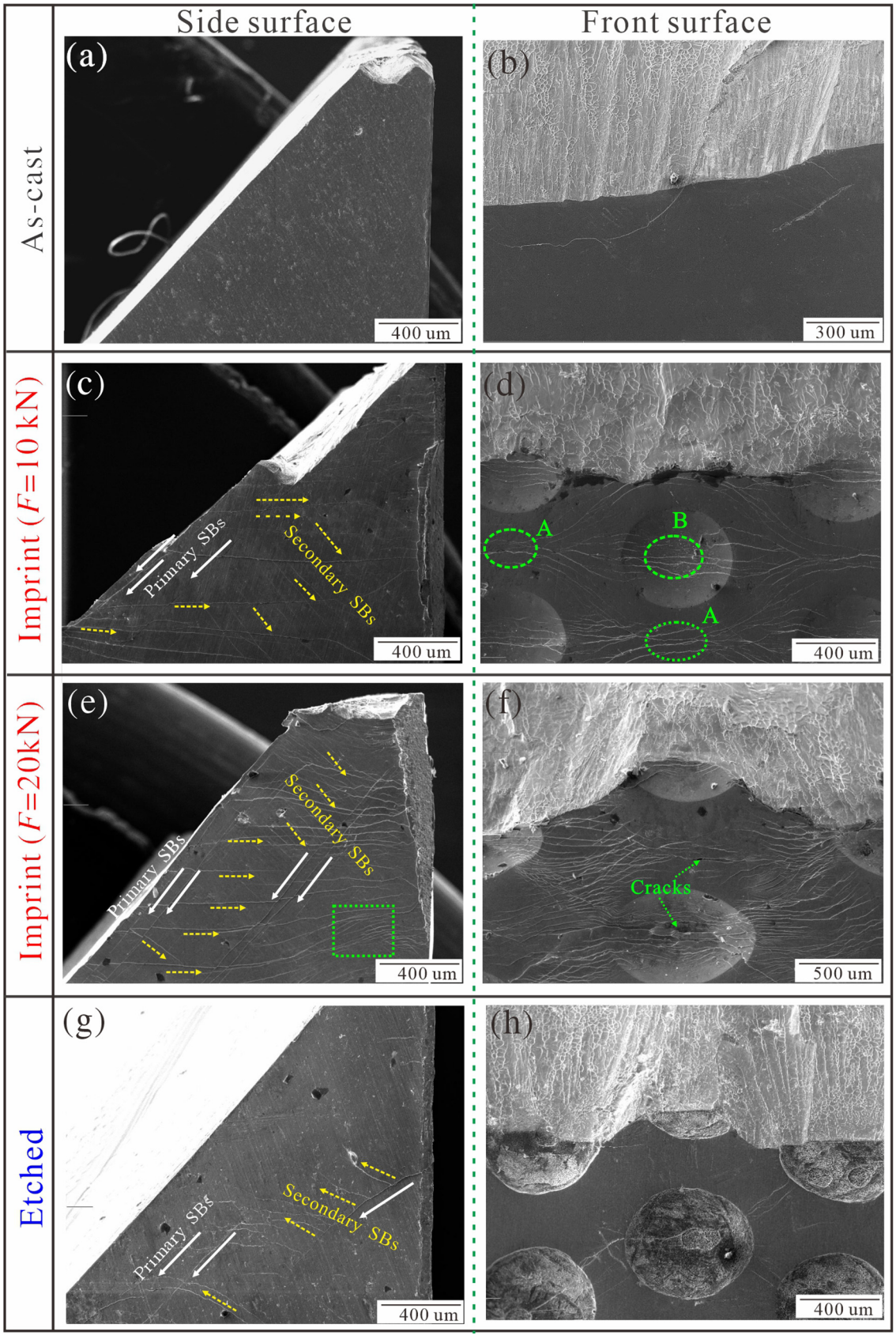


**Fig. 5.** SEM micrographs of the fractured surfaces of (a)-(f) the imprinted MG samples prepared under different applied imprinting forces (i.e., $F = 0$ kN, 10 kN and 20 kN, respectively) and (g)-(h) the etched MG sample after uniaxial compression. The first column and second column show the fractured side surfaces and front surfaces of these samples, respectively. The primary and secondary shear bands (SBs) on the fractured side surfaces were highlighted by the solid white arrows and the dotted yellow arrows, respectively.

## 4. Discussion

As observed in the experiments, residual stress improves the mechanical properties of the imprinted MGs via promoting the nucleation of multiple shear bands upon yielding near the imprinted surfaces as well as inducing deflection and branching of shear bands when they propagate in the interior of the samples. However, the underlying mechanisms are still unclear. In the following sections, we turn to examine the mechanisms using both FEM and MD analysis.

### 4.1. Effect of residual stress on shear band nucleation

We first examined how the residual stress affects the shear band nucleation in the imprinted MGs at the early plastic deformation stage. Due to the glassy nature of MGs, it is difficult to measure the internal residual stresses in MGs using experimental approaches like in crystalline metals [11]. As an alternative, FEM analysis was adopted. The residual stress distribution after surface imprinting was investigated. Uniaxial compression simulations were further performed to comparatively study the yield behavior of the imprinted and etched MG models based on the analysis of the distributions of the equivalent stress, through which the effects of residual stress on the nucleation of multiple shear bands in the imprinted MGs can be illuminated appropriately.

Fig. 6(a) schematically illustrates the 2D geometric model used for simulating the imprinted and etched MGs in the FEM analysis, both of which were set to have the same pit depth of 76 μm, i.e., the value of the depth produced in the MG imprinted at $F = 20$ kN. Fig. 6(b) depicts the contour map of the residual stress along the Y-direction ($\sigma^Y$) in the imprinted model. Here, $\sigma^Y$ was chosen for analysis since its direction coincides with the direction of the applied force under the subsequent uniaxial compression, and has the most significant influence on the deformation behavior of the samples as compared with other stress components [11]. One can see from Fig. 6(b) that the inner region of the imprinted model suffers from tensile residual stresses, whereas the imprinted surfaces are in compressive residual stresses. The generation of compressive residual stresses near the treated surfaces of MGs has been widely reported in various other mechanical surface pretreatments, such as shot peening, surface attrition treatment and cold rolling [29,31,61]. However, the compressive residual stress near the imprinted surfaces has a more complex distribution in surface imprinting due to the characteristics of the local plastic deformation in this treatment [57]. More specifically, the compressive residual stresses reach the local maximum periodically at two characteristic locations near the imprinted surfaces: one is below the bottom of each pit, and the other is in the middle regions between the adjacent pits (i.e., the two blue regions marked as A and B in Fig. 6(b), respectively).

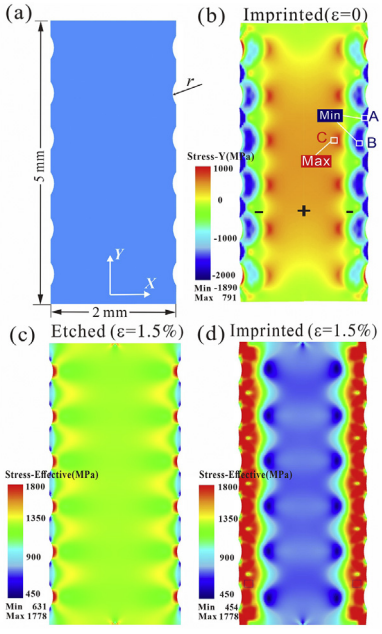


**Fig. 6.** FEM analysis of the deformation mechanisms of the imprinted and etched FEM models. (a) Schematic of the geometrical shape of the imprinted and etched models. (b) The contour map of the residual stress along the loading direction ($\sigma^Y$) in the imprinted model. (c)-(d) The contour maps of von Mises stress ($\sigma_{Mises}$) in the etched and imprinted models at the compressive strain of 1.5%.

Fig. 6(c)–(d) demonstrates the contour maps of the equivalent stress ($\sigma_{eq}$) in the etched and imprinted models under a compressive strain of 1.5%. The areas mapped with the color close to red indicate materials that suffer from high equivalent stresses and tend to experience early plastic deformation [17]. One can see that, for the etched model (the reference), high equivalent stresses were only observed at the bottom of etched pits due to stress concentration raising from the geometric pits. However, in the imprinted model, much larger regions near the imprinted surfaces underwent high stresses. As revealed in Fig. 6(b), the residual stress in the inner region of the imprinted model was in tensile states, whereas the imprinted surfaces are in compressive states. When the imprinted model is further compressed under uniaxial compressive loading, the local compressive residual stresses near the imprinted surfaces superimposed the applied compressive stress, while the tensile residual stresses in the inner region counteracted the applied compressive stress at the early deformation stage [11]. This resulted in an obvious stress gradient between the inner region and the imprinted surfaces, which induced earlier yielding of the materials near the imprinted surfaces, while the inner region was still in the elastic deformation state. Meanwhile, due to the local maximum compressive residual stresses, region A and region B were inclined to yield earliest, acting as preferential nucleation sites for multiple shear bands on the surfaces at the early deformation stage. This explains why a high density of shear bands can be observed in the corresponding regions (also marked as A and B in Fig. 5(d)) on the deformed surfaces of the imprinted MGs in experiments. In addition, since the pits were imprinted into dense AB-stacked patterns in the experiments, a network of shear bands that both surrounds and penetrates the pits can be thus observed in the imprinted MGs (Fig. 5(d) and Fig. 5(f)). From these FEM analyses, it is clear that compressive residual stresses near the surfaces induce obvious stress gradients and highly heterogeneous deformation, thus facilitating the formation of multiple shear bands at the early deformation stage.

To illustrate the *F*-dependent mechanical properties observed in the experiments, Fig. 7 depicts the spatial distributions of $\sigma^Y$ as a function of the distance from the center of symmetry along the X-direction in four imprinted models. The imprinting depths of these models were 38 μm, 56 μm, 76 μm and 91 μm, which correspond to the cases of experimentally imprinted MGs prepared with $F = 10$ kN, 15 kN, 20 kN and 25 kN, respectively. As such, we can quantitatively estimate the residual stress evolution in the imprinted MGs. The local value of $\sigma^Y$ was calculated using the formula: $\sigma^Y(x) = \sum_{i=1}^{N(x)} \sigma_i^Y / N(x)$, where $\sigma_i^Y$ is the Y-direction component of the stress tensor of elemental node *i*, and $N(x)$ is the number of elemental nodes within the binned shell between $x$ and $x + \Delta x$. One can see from Fig. 7 that, with increasing the imprinting depth or force, both the compressive residual stress near the surfaces and the tensile residual stress in the inner region increase progressively. Apparently, this would lead to a larger stress gradient in the transition region (i.e., the locations around $x \approx 0.7$–$0.9$ mm). As explained above, the compressive residual stress near the surfaces induces a stress gradient upon loading, which can induce an early yielding of the materials near the surfaces and, thus, promote the formation of multiple shear bands at the early plastic deformation stage. The inner region deforms elastically in a cooperative manner at this stage. With increasing compressive residual stress near the surfaces in the imprinted MGs, the deformation between the inner region and the surface tends to be more

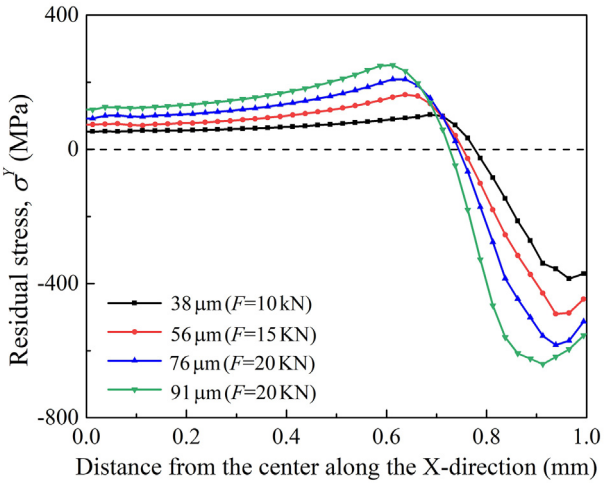


**Fig. 7.** Spatial distributions of the local residual stress, $\sigma^Y$, as a function of the distance from the symmetry center along the X-direction in the series of imprinted models. The bin size, $\Delta x$, was 0.025 mm.

heterogeneous due to the larger stress gradient under compressive loading. Therefore, for MGs imprinted with higher *F*, more shear bands are expected to be initiated from the imprinted surfaces before the occurrence of plastic deformation in the inner region.

### 4.2. Effect of residual stress on shear band propagation

After the formation of shear bands from the surfaces, some will propagate to the inner region with further deformation to accommodate the global plasticity throughout the samples. Due to the presence of residual stresses in the imprinted MGs, these shear bands will penetrate across some regions with apparent stress gradients. Their shear banding behavior may be greatly affected by the stress gradient, hindering the generation of a detrimental shear band throughout the sample [24,36]. One indeed can observe deflection and branching of many shear bands on the side surfaces (see Fig. 5(e)) when they propagate in the interior of the imprinted MGs. The above FEM analysis cannot fully assess the influence of residual stress (or the resultant stress gradient) on the detailed shear banding process. As an alternative, complementary MD simulations were conducted. The nanosized S-MGs adopted in atomistic simulations can be regarded as a representative volume of the transition regions suffering from different levels of residual stresses in the imprinted MGs. As such, we can establish physical links between the atomistic simulations and the experiments. Through compressing these S-MGs without/with tailored residual stresses, the effect of residual stresses on the shear band propagation and its underlying mechanisms can be uncovered.

Fig. 8(a) and (c) display the atomic configurations of the M-MG and the S-MG prepared with a pre-loading strain $\Delta\varepsilon$ of 3%. For clarity, regions that suffered from different levels of residual stresses were highlighted using different colors in the S-MG. The upper insets of Fig. 8(a) and (c) describe the variations of the Cu-centred FI fraction along the X-direction in the M-MG and S-MG, respectively. The similar distribution of the Cu-centred FI fraction in these two models indicated that elastic pre-straining, which was applied to induce residual stresses in the sample preparation process, barely influenced the structural disordering degree. The lower insets of Fig. 8(a) and (c) present the variations of the local residual stress along the Y-direction ($\sigma^Y$). The M-MG is almost free from residual stress due to its as-quenched structure, whereas the S-MG displays an obvious compressive residual stress (−1.7 GPa) in the left half part and a tensile residual stress (+1.7 GPa) in the right half part. Meanwhile, a narrow transition zone (~4 nm in thickness) with a significant stress gradient exists between the two parts. For all the S-MGs, the profiles of the residual stresses were nearly the same, with only differences in their amplitudes. Therefore, the S-MGs can be regarded as structurally homogeneous but mechanically heterogenous MGs, which allow us to directly evaluate the effect of the residual stress on the shear banding behavior. More details of the structural characterization and residual stress analysis are provided in the Supplementary Materials.

Fig. 8(b) and (d) demonstrate the plastic deformation process of the M-MG and the S-MG with $\sigma_0 = 1.7$ GPa (i.e., the one prepared with $\Delta\varepsilon = 3\%$) monitored by $\eta^{Mises}$. For the residual stress-free M-MG, an embryonic shear band was initiated from the bottom of the notch at $\varepsilon = 5.5\%$ when STZs aggregate to a critical size comparable to the width of shear bands (5– 10 nm) [53]. At higher loads, the shear band propagated rapidly to the right surface almost along the maximum shear plane and penetrated the entire sample at $\varepsilon = 6.2\%$ (see Supplementary Video S1). The corresponding strain increment for the shear band propagation was found to be as low as 0.7%. The rapid propagation of the individual shear band through the sample over small strain increments is generally viewed as a characteristic of poor plasticity in MGs [62]. However, the situation altered in the S-MGs tailored with residual stresses. For the S-MG with $\sigma_0 = 1.7$ GPa, the corresponding strain increment for the shear band propagation was enlarged to a value as high as 4.4%, i.e., from an applied strain of 2.8% to 7.1% (Fig. 8(d)). The shear band was initiated much earlier in the S-MG due to the presence of large compressive residual stresses in its left part. When it rapidly penetrated to the stress-transition region with apparent stress gradient (i.e., the area near the white dotted line in Fig. 8(d)), its propagation appeared to be suppressed (see Supplementary Video S2). With further deformation, its propagating front became thicker via the local strain concentration near the transition region, and shear branching then occured (see the white arrows in Fig. 8(d) at $\varepsilon = 5.9\%$). During this process, new embryonic shear bands were even generated in the left part to accommodate the increase of the applied strain. Apparently, the stress gradient was unfavorable for the rapid propagation of shear bands [24,30]. Only when the applied strain was sufficiently large, one shear band bifurcated from the initial shear front began to propagate to the right half part and soon penetrated the whole sample (see $\varepsilon = 7.1\%$ in Fig. 8(d)), forming a mature shear band. These findings suggest that, apart from facilitating the formation of multiple shear bands at the early deformation stage as also revealed by FEM analysis, the residual stresses also play a vital role in suppressing the propagation of the shear bands via shear band branching in the region with an obvious stress gradient, finally giving rise to the improved plasticity of the glass.

To qualitatively evaluate the shear banding dynamics in the S-MGs, the lengths of the main shear bands along the propagating direction ($L_{SB}$, see Fig. 8(b) and (d)) were measured as a function of the applied strain ($\varepsilon$) in the S-MGs tailored with different levels of residual stresses (i.e., $\sigma_0 = 0$ GPa, 0.7 GPa, 1.3 GPa and 1.7 GPa, respectively). The results are presented in Fig. 9. The slope in the $L_{SB}$-$\varepsilon$ curves at any $\varepsilon$ can be taken as the propagating speed of the primary shear band at the corresponding moment. It is seen that the shear banding process in the M-MG (i.e., $\sigma_0 = 0$ GPa) can be roughly divided into two stages, i.e., an initial stage for shear band initiation followed by another stage for rapid shear band propagation. The rapid propagation of the main shear band in the M-MG originates from the lack of microstructures such as lattice dislocations and grain boundaries that induces strain hardening observed in crystalline metals [18]. The discovery of two shear banding stages in the M-MG is in accord with previous MD simulation studies on monolithic MGs [48,63]. While, for the structurally homogeneous but mechanically heterogenous S-MGs, there apparently exists four stages in the whole shear banding process. More specifically, an extra stage for shear band suppression is clearly present in the middle of the shear banding process (i.e., corresponding to the range of $L_{SB}$ between 37– 47 nm, as shown in Fig. 9). One can see that, regardless of the levels of residual stresses in the S-MGs, the shear banding speeds at the rapid propagation stages (i.e., when the main shear band extends in the left

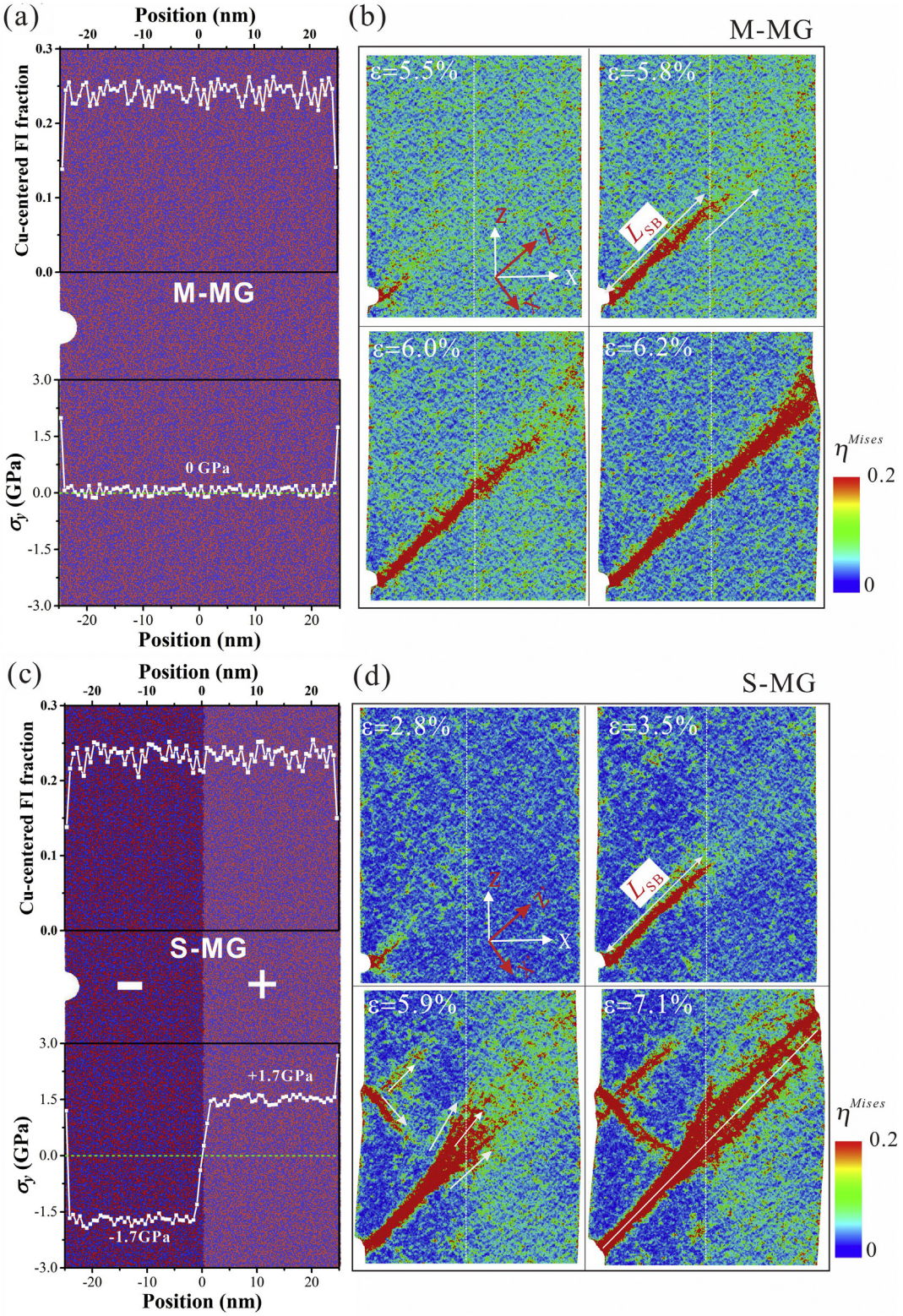


**Fig. 8.** Shear banding process in the simulated MGs with/without residual stresses. (a) and (c) demonstrate the atomic configurations of the M-MG and S-MG, respectively; The upper and lower insets in (a) and (c) show the distributions of the Cu-centered FI fraction and the residual stress ($\sigma^y$) as a function of the position along the X-direction. (b) and (d) present the shear banding process in the M-MG and S-MG, respectively. The dashed lines denote the boundary between the negatively and positively stressed domains in the samples. The white arrows in (d) at $\varepsilon = 5.9\%$ denote the generated embryonic shear bands and branches. The white line in (d) at $\varepsilon = 7.1\%$ marks the direction of the initial shear band in the left part. The atoms in (b) and (d) are colored according to their values of $\eta^{Mises}$.

and right half parts) are almost the same as that of the M-MG. While, the corresponding speed at the suppression stage (i.e., when the primary shear band extends in the stress-transition region) decreases gradually with increasing the levels of tailored residual stresses. These imply that the shear banding behavior in the glass matrix is barely affected by the uniformly distributed stresses in the negatively and positively stressed

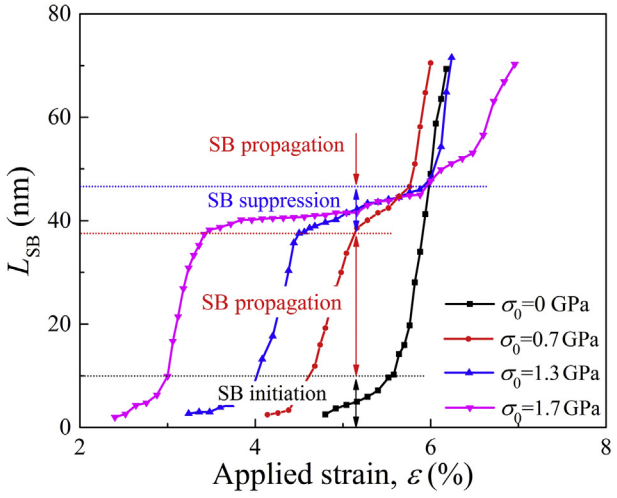


**Fig. 9.** The evolution of the length ($L_{SB}$) of the dominating shear band (SB) in the simulated S-MGs tailored with different levels of residual stresses.

parts but governed by the stress gradient in the middle stress-transition region. With increasing the stress gradient in the stress-transition region, the suppressing effect of the stress gradient on the shear banding behavior tends to be more apparent via shear band branching, and new shear bands can be even promoted simultaneously (see the shear band patterns in the series of S-MGs in Supplementary Fig. S5). Therefore, one can see a tendency for more delocalized plastic deformation via shear band branching around the middle stress-transition region in the S-MGs with increasing the level of stress gradient. Strain delocalization via shear band branching impedes the formation of a fatal shear band and retards runaway instability [62]. It also promotes the energy barrier and the stress required for the propagation of the primary shear bands that penetrate the whole MG. These findings explain why the imprinted MGs with residual stresses demonstrate a simultaneous improvement of plasticity and strength as observed in the experimental data (Fig. 3).

Finally, we turn to examine the reasons why the stress gradient raised from the residual stresses is so effective in slowing down the shear banding dynamics and promoting shear band branching. To this end, we comparatively examined the atomic-level shear banding process in the M-MG and the S-MG prepared with $\sigma_0 = 1.7$ GPa. Fig. 10(a) presents the distributions of the atomic shear stress along the shear path (i.e., along the X′-axis) in the M-MG and the S-MG at the state before deformation, which clearly demonstrate the uniform and nonuniform characteristics of the stress distributions in the two simulated MGs. Fig. 10(b)–(c) display the evolutions of the atomic shear strain ($\eta^{Misses}$, the left panels) and the rotation angle ($W$, the right panels) of the M-MG and the S-MG upon loading. To better visualize the detailed deformation process, these two parameters are presented as the increments measured with a strain interval of 0.12%. One can see that, for the M-MG (see Fig. 10(b)), strain accumulations built up over the strain interval are highly discontinuous within the single shear band. Isolated regions with large $\eta^{Misses}$ (i.e., STZs) and isolated regions with strong rotation (i.e., vortex-like units) but small $\eta^{Misses}$ can be clearly identified within the shear bands, specifically at the shear front. More specifically, the strong strain field associated with the STZs and the strong rotational field associated with the vortexes seems to be mutually exclusive. The observed STZ-vortex units in the process of shear band formation in the M-MG is consistent with the atomistic studies conducted by Sopu et al. [56,62,64], who found the activation of the STZ-vortex sequence controls the shear banding dynamics in MGs. It was reported that STZs behave like Eshelby inclusions, which can induce collective vortex-like motions in the shear front [64,65]. Upon successive loading, the vortex-like motions in turn act as medium, triggering the activation of successive STZs [56,64]. In such a way, the repetition of STZ-vortex arrangements in the shear front (see the dashed boxes in Fig. 10(b)) leads to the autocatalytic percolation of STZs and finally causes the rapid propagation of the shear band in the M-MG. Due to the absence of any accountable heterogeneities in the M-MG, the shear band tends to propagate unimpededly along the preferential maximum shear stress plane, i.e., along the X′-axis (see the arrow in Fig. 10(b)). Thus, one can only see one single shear band with fast propagation dynamics in the M-MG.

For the mechanically heterogeneous S-MG, however, the stress changes significantly in the middle stress-transition region (See the region between the dotted lines in the right panel of Fig. 10(a)). Since shear banding behavior is a stress-driven process [21], the presence of such local stress changes in the stress-transition region may affect the STZ-vortex formation process ahead of the shear band. The evolutions of $\eta^{Misses}$ and $W$ in Fig. 10(c) reveal that, in the left part of the S-MG with uniformly distributed compressive residual stress, the percolation of STZs, i.e., the propagation of the shear band, is almost along the preferential X′-axis (see $\varepsilon = 3.32\%$ and 3.68% in Fig. 10(c)), similar to that observed in the M-MG. However, when the shear front approaches the middle stress-transition region, the continuous STZ percolation along the X′-axis tend to be hampered. This may be due to the modification of the local stress field in the shear front caused by the stress gradient in the stress-transition region. It is accepted that a critical stress is needed for the activation and percolation of STZs in MGs, reminiscent of the scenario for the nucleation and movement of dislocations in crystalline metals. Apparently, the stress gradient in the stress-transition region leads to obvious local stress drops along the shear path, which greatly reduce the local stress for STZ percolation and thus slow down the shear banding dynamics. Upon further loading, the local stress in the shear front is expected to increase gradually and at a certain point it may be sufficient for the growth of the existing shear band across the stress-transition region. However, due to the high internal stress in the left half part, the formation of new STZ-vortex sequences (see one indicated by the arrow at $\varepsilon = 3.68\%$ in Fig. 10(c)) near the stress-transition region is favored over the growth of the existing shear band across the stress-transition region. These newly formed STZ-vortex sequences deviate from the maximum shear stress plane, thickening the shear front near the stress-transition region and resulting in a finger-like pattern (see Fig. 8(d)). They also have the possibility for extending across the stress-transition region and propagating as new embryonic shear bands in the right half part when the local stress in the stress-transition region is sufficient for shear band propagation. The snapshot shown at $\varepsilon = 7.20\%$ in Fig. 10(c) clearly demonstrates that two shear band branches were successfully extended from the finger-like pattern with their propagation direction in the right half part almost along the X′-axis.

Through the above comparison, we can see that the stress gradient raised from the residual stresses in the S-MG can effectively change the autocatalytic percolation of STZs in the shear front, which consequently slow down the shear banding dynamics and lead to shear band branching in the S-MG. The effect of the stress gradient in the shear banding process is somewhat analogous to the interactions between the shear bands and structural heterogeneities, which were also found to be able to effectively promote shear band deflection and branching due to the changes of the local stress field caused by the structural heterogeneities [56,62]. It should be noted that surface imprinting always induces a complex multi-axial residual stress field in the imprinted MGs. Although only one component of the residual stresses which coincides with the direction of the applied force is considered in the nanoscale MD simulation, the simplified model is adequate in capturing the underlying mechanisms as to how the stress gradient raised from the residual stresses affects the shear banding behavior in the imprinted MGs. Finally, it should be pointed out that the models in the MD simulations only have sizes of tens of nanometers, and only one shear band was induced intentionally by installing a small notch on the surfaces of the models for the simplicity of analysis.

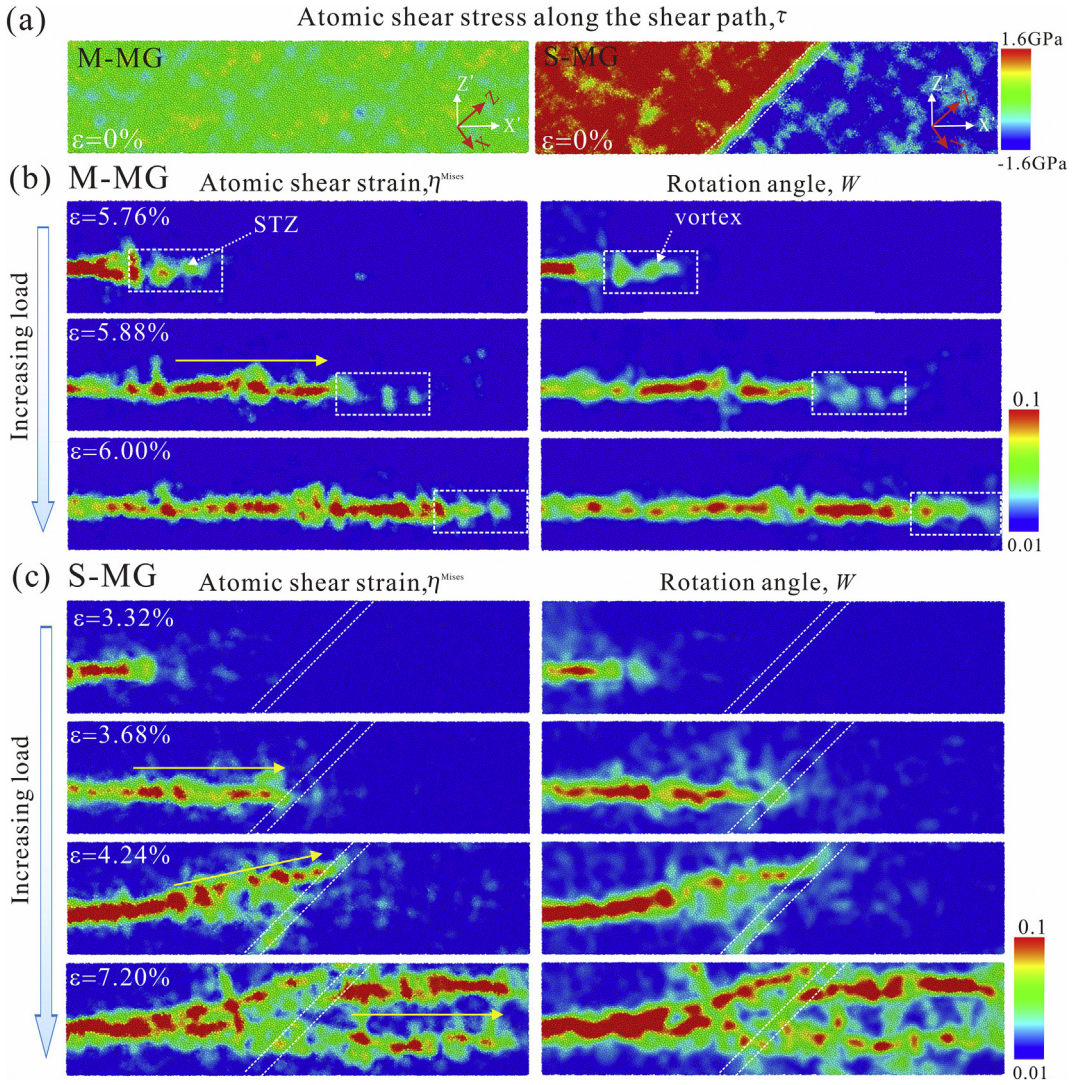


**Fig. 10.** (a) Distributions of the atomic shear stress along the shear path ($\tau$) prior to deformation in the simulated M-MG and the S-MG with $\sigma_0 = 1.7$ GPa, respectively. The X- and X′-axis indicate the loading direction and shear path, respectively. (b) and (c) Evolutions of the atomic shear strain ($\eta^{Misses}$) and rotation angle ($W$) upon loading in the simulated M-MG and the S-MG with $\sigma_0 = 1.7$ GPa, respectively. The areas between the two dotted lines indicate the stress-transition region in the S-MG. The arrows in (b) and (c) indicate the directions of the STZ-vortex sequences formed at different applied strains.

Therefore, the present MD models can only capture the early stages of the deflection and branching of one single shear band during its propagation. Nevertheless, the process of shear band deflection and branching would further develop and extend at the macro-scale if shear bands are not confined in the nanosized zone.

## 5. Conclusions

The plastic deformation behaviours of several tailored MGs (i.e., the imprinted and etched samples) were comparatively investigated with the aid of experimental and computational methods. Valuable insights were gained into understanding the effects of the residual stress on the initiation, propagation and multiplication of shear bands in structurally homogeneous but mechanically heterogenous MGs, as well as the underlying mechanisms of the improved mechanical properties. It was found that, compared to the etched and as-cast counterparts, the imprinted MGs exhibit a simultaneous improvement of plasticity and ultimate strength. Moreover, a good combination of enhanced plasticity and ultimate strength in the imprinted MGs can be controllably tuned by appropriate selection of $F$ in the surface imprinting process. The enhanced mechanical properties observed in the imprinted MGs are mainly ascribed to the compressive residual stresses generated near the surfaces after surface imprinting, rather than the resultant geometrical pits. FEM simulations further illustrated that the compressive residual stress near the surfaces in the imprinted MGs promotes earlier yielding of material at the bottom region of the indented pits and regions between the pits, which act as heterogeneous nucleation sites for multiple shear bands at the early plastic deformation stage. Further, MD simulations revealed that the stress gradient raised from the residual stresses can effectively change the characteristic of autocatalytic percolation of STZs in the shear front observed in the M-MG, which consequently slows down the shear banding dynamics and leads to shear band deflection and branching. The findings of this study establish a clear physical relationship between residual stresses/stress gradient and the mechanical properties of MGs, which are useful for processing MGs with desirable mechanical properties for practical applications.

Supplementary data to this article can be found online at https://doi.org/10.1016/j.matdes.2020.109246.

## Data availability

All relevant data are available from authors upon reasonable request.

## CRediT authorship contribution statement

**Lei Zhao:** Conceptualization, Methodology, Software, Data curation, Writing - original draft and Writing - review & editing. **DongXue Han**, **Shuai Guan** and **Xianzheng Lu:** Methodology, Software and Validation. **Gang Wang:** Methodology, Formal analysis and Writing-Review & Editing. **Kangcheung Chan:** Writing-review & editing, Supervision, Project administration and Funding acquisition.

## Declaration of Competing Interest

The authors declare that they have no known competing financial interests or personal relationships that could have appeared to influence the work reported in this paper.

## Acknowledgements

This work described in this paper was fully supported by the Faculty of Engineering of The Hong Kong Polytechnic University under the account No. 1-45-37-99QP.

## References

[1] W.H. Wang, C. Dong, C.H. Shek, Bulk metallic glasses, Mater. Sci. Eng. R 44 (2–3) (2004) 45–90.
[2] C.A. Schuh, T.C. Hufnagel, U. Ramamurty, Mechanical behavior of amorphous alloys, Acta Mater. 55 (12) (2007) 4067–4109.
[3] J. Zhou, Q. Wang, X. Hui, Q. Zeng, Y. Xiong, K. Yin, B. Sun, L. Sun, M. Stoica, W. Wang, B. Shen, A novel FeNi-based bulk metallic glass with high notch toughness over 70 MPa m1/2 combined with excellent soft magnetic properties, Mater. Des. 191 (2020).
[4] N.T. Panagiotopoulos, K. Georgarakis, A.M. Jorge Jr., M. Aljerf, W.J. Botta, A.L. Greer, A.R. Yavari, Advanced ultra-light multifunctional metallic-glass wave springs, Mater. Des. 192 (2020).
[5] B.A. Sun, W.H. Wang, The fracture of bulk metallic glasses, Prog. Mater. Sci. 74 (2015) 211–307.
[6] M.M. Trexler, N.N. Thadhani, Mechanical properties of bulk metallic glasses, Prog. Mater. Sci. 55 (8) (2010) 759–839.
[7] A. Inoue, A. Takeuchi, Recent development and application products of bulk glassy alloys, Acta Mater. 59 (6) (2011) 2243–2267.
[8] C. Ma, S. Suslov, C. Ye, Y. Dong, Improving plasticity of metallic glass by electropulsing-assisted surface severe plastic deformation, Mater. Des. 165 (2019).
[9] T. Wang, Y. Wu, J. Si, Y. Liu, X. Hui, Plasticizing and work hardening in phase separated Cu-Zr-Al-Nb bulk metallic glasses by deformation induced nanocrystallization, Mater. Des. 142 (2018) 74–82.
[10] Y. Cheng, S. Pang, C. Chen, T. Zhang, Tensile plasticity in monolithic bulk metallic glass with sandwiched structure, J. Alloys Compd. 688 (2016) 724–728.
[11] L. Zhao, K. Chan, S. Feng, X. Lu, S. Chen, G. Wang, Atomistic understanding of deformation-induced heterogeneities in wire drawing and their effects on the tensile ductility of metallic glass wires, J. Alloys Compd. 803 (2019) 193–204.
[12] R. Qu, S. Wu, S. Wang, X. Wang, Z. Zhang, Shear banding stability and fracture of metallic glass: effect of external confinement, J. Mech. Phys. Solids 103922 (2020).
[13] V.S. Saji, Electrodeposition in bulk metallic glasses, Materialia 3 (2018) 1–11.
[14] R.T. Qu, S.G. Wang, X.D. Wang, S.J. Wu, Z.F. Zhang, Shear band fracture in metallic glass: sample size effect, Mater. Sci. Eng. A 739 (2019) 377–382.
[15] C.A. Volkert, A. Donohue, F. Spaepen, Effect of sample size on deformation in amorphous metals, J. Appl. Phys. 103 (8) (2008), 083539, .
[16] J. Pan, Y.X. Wang, Y. Li, Ductile fracture in notched bulk metallic glasses, Acta Mater. 136 (2017) 126–133.
[17] J.X. Zhao, Achieving the desirable compressive plasticity by installing notch cluster in metallic glass, Mater. Sci. Eng. A 634 (2015) 134–140.
[18] L. Zhao, K.C. Chan, S.H. Chen, Atomistic deformation mechanisms of amorphous/polycrystalline metallic nanolaminates, Intermetallics 95 (2018) 102–109.
[19] L. Zhang, S. Chen, H.M. Fu, H. Li, Z.W. Zhu, H.W. Zhang, Z.K. Li, A.M. Wang, H.F. Zhang, Tailoring modulus and hardness of in-situ formed β-Ti in bulk metallic glass composites by precipitation of isothermal ω-Ti, Mater. Des. 133 (2017) 82–90.
[20] Z.J. Ma, Y.C. Guo, L.T.L. Yeung, P.H. Gao, Z. Yang, X.R. Zeng, The effect of cooling rate on the plasticity of amorphous metal, J. Alloys Compd. 648 (2015) 18–21.
[21] L. Zhao, K.C. Chan, S.H. Chen, S.D. Feng, D.X. Han, G. Wang, Tunable tensile ductility of metallic glasses with partially rejuvenated amorphous structures, Acta Mater. 169 (2019) 122–134.
[22] K.K. Song, S. Pauly, Y. Zhang, S. Scudino, P. Gargarella, K.B. Surreddi, U. Kuhn, J. Eckert, Significant tensile ductility induced by cold rolling in Cu47.5Zr47.5Al5 bulk metallic glass, Intermetallics 19 (10) (2011) 1394–1398.
[23] M.H. Lee, K.S. Lee, J. Das, J. Thomas, U. Kühn, J. Eckert, Improved plasticity of bulk metallic glasses upon cold rolling, Scr. Mater. 62 (9) (2010) 678–681.
[24] S.H. Chen, K.C. Chan, L. Xia, Effect of stress gradient on the deformation behavior of a bulk metallic glass under uniaxial tension, Mater. Sci. Eng. A 574 (2013) 262–265.
[25] S. Chen, L. Zhang, H.M. Fu, Z.K. Li, Z.W. Zhu, H. Li, H.W. Zhang, A.M. Wang, Y.D. Wang, H.F. Zhang, Compressive mechanical properties and failure modes of Zr-based bulk metallic glass composites containing tungsten springs, Mater. Des. 160 (2018) 652–660.
[26] K.K. Song, X.L. Han, S. Pauly, Y.S. Qin, K. Kosiba, C.X. Peng, J.H. Gong, P.X. Chen, L. Wang, B. Sarac, S. Ketov, M. Mühlbacher, F. Spieckermann, I. Kaban, J. Eckert, Rapid and partial crystallization to design ductile CuZr-based bulk metallic glass composites, Mater. Des. 139 (2018) 132–140.
[27] D. Uhlmann, Elasticity and Strength in Glasses: Glass: Science and Technology, Elsevier, 2012.
[28] J. Zarzycki, Glasses and the Vitreous State, Cambridge University Press, 1991.
[29] Y. Zhang, W.H. Wang, A.L. Greer, Making metallic glasses plastic by control of residual stress, Nat. Mater. 5 (11) (2006) 857–860.
[30] L. Wang, L. Wang, Z. Nie, Y. Ren, Y. Xue, R. Zhu, H. Zhang, H. Fu, Evolution of residual stress, free volume, and hardness in the laser shock peened Ti-based metallic glass, Mater. Des. 111 (2016) 473–481.
[31] Q. Wang, Y. Yang, H. Jiang, C.T. Liu, H.H. Ruan, J. Lu, Superior tensile ductility in bulk metallic glass with gradient amorphous structure, Sci. Rep. 4 (2014) 4757.
[32] Y. Cao, X. Xie, J. Antonaglia, B. Winiarski, G. Wang, Y.C. Shin, P.J. Withers, K.A. Dahmen, P.K. Liaw, Laser shock peening on zr-based bulk metallic glass and its effect on plasticity: experiment and modeling, Sci. Rep. 5 (2015) 10789.
[33] B. Chen, Y. Li, M. Yi, R. Li, S. Pang, H. Wang, T. Zhang, Optimization of mechanical properties of bulk metallic glasses by residual stress adjustment using laser surface melting, Scr. Mater. 66 (12) (2012) 1057–1060.
[34] B. Chen, S. Pang, P. Han, Y. Li, A.R. Yavari, G. Vaughan, T. Zhang, Improvement in mechanical properties of a Zr-based bulk metallic glass by laser surface treatment, J. Alloys Compd. 504 (2010) S45–S47.
[35] Y. Cheng, S. Pang, C. Chen, T. Zhang, Tailoring residual stress to achieve large plasticity in Zr55Al10Ni5Cu30bulk metallic glass, J. Alloys Compd. 690 (2017) 176–181.
[36] F. Haag, D. Beitelschmidt, J. Eckert, K. Durst, Influences of residual stresses on the serrated flow in bulk metallic glass under elastostatic four-point bending - a nanoindentation and atomic force microscopy study, Acta Mater. 70 (2014) 188–197.
[37] R.Q. Yang, J.T. Fan, S.X. Li, Z.F. Zhang, Fracture behavior of Zr55Cu30Al10Ni5 bulk metallic glass under quasi-static and dynamic compression, J. Mater. Res. 23 (6) (2008) 1744–1750.
[38] N. Van Steenberge, A. Concustell, J. Sort, J. Das, N. Mattern, A. Gebert, S. Suriñach, J. Eckert, M.D. Baró, Microstructural inhomogeneities introduced in a Zr-based bulk metallic glass upon low-temperature annealing, Mater. Sci. Eng. A 491 (1–2) (2008) 124–130.
[39] A.M. Korsunsky, T. Sui, E. Salvati, E.P. George, M. Sebastiani, Experimental and modelling characterisation of residual stresses in cylindrical samples of rapidly cooled bulk metallic glass, Mater. Des. 104 (2016) 235–241.
[40] B. Sarac, J. Schroers, Designing tensile ductility in metallic glasses, Nat. Commun. 4 (2013).
[41] M. Gao, J. Dong, Y. Huan, Y.T. Wang, W.H. Wang, Macroscopic tensile plasticity by scalarizating stress distribution in bulk metallic glass, Sci. Rep. 6 (2016).
[42] S.H. Chen, K.C. Chan, D.X. Han, L. Zhao, F.F. Wu, Programmable super elastic kirigami metallic glasses, Mater. Des. 169 (2019).
[43] D. Han, L. Zhao, S. Chen, G. Wang, K. Chan, Critical transitions in the shape morphing of kirigami metallic glass, J. Mater. Sci. Technol. 61 (2021) 204–212.
[44] S.H. Chen, K.C. Chan, T.M. Yue, F.F. Wu, Highly stretchable kirigami metallic glass structures with ultra-small strain energy loss, Scr. Mater. 142 (2018) 83–87.
[45] S. Plimpton, Fast parallel algorithms for short-range molecular dynamics, J. Comput. Phys. 117 (1) (1995) 1–19.
[46] Y.Q. Cheng, E. Ma, H.W. Sheng, Atomic level structure in multicomponent bulk metallic glass, Phys. Rev. Lett. 102 (24) (2009) 245501.
[47] W. Shinoda, M. Shiga, M. Mikami, Rapid estimation of elastic constants by molecular dynamics simulation under constant stress, Phys. Rev. B 69 (13) (2004).
[48] A.J. Cao, Y.Q. Cheng, E. Ma, Structural processes that initiate shear localization in metallic glass, Acta Mater. 57 (17) (2009) 5146–5155.
[49] F. Shimizu, S. Ogata, J. Li, Theory of shear banding in metallic glasses and molecular dynamics calculations, Mater. Trans. 48 (11) (2007) 2923–2927.
[50] A. Stukowski, Visualization and analysis of atomistic simulation data with OVITO-the Open Visualization Tool, Model. Simul. Mater. Sci. Eng. 18 (1) (2009), 015012, .
[51] S. González, J. Fornell, E. Pellicer, S. Suriñach, M.D. Baró, A.L. Greer, F.J. Belzunce, J. Sort, Influence of the shot-peening intensity on the structure and near-surface mechanical properties of Ti40Zr10Cu38Pd 12 bulk metallic glass, Appl. Phys. Lett. 103 (21) (2013).
[52] R.T. Qu, Q.S. Zhang, Z.F. Zhang, Achieving macroscopic tensile plasticity of monolithic bulk metallic glass by surface treatment, Scr. Mater. 68 (11) (2013) 845–848.
[53] Z. Sha, Y. Teng, L.H. Poh, Q. Pei, G. Xing, H. Gao, Notch strengthening in nanoscale metallic glasses, Acta Mater. 169 (2019) 147–154.
[54] Z.D. Sha, Q.X. Pei, Z.S. Liu, Y.W. Zhang, T.J. Wang, Necking and notch strengthening in metallic glass with symmetric sharp-and-deep notches, Sci. Rep. 5 (2015).
[55] X. Lei, C. Li, X. Shi, X. Xu, Y. Wei, Notch strengthening or weakening governed by transition of shear failure to normal mode fracture, Sci. Rep. 5 (2015).
[56] D. Sopu, S. Scudino, X.L. Bian, C. Gammer, J. Eckert, Atomic-scale origin of shear band multiplication in heterogeneous metallic glasses, Scr. Mater. 178 (2020) 57–61.

[57] S. Scudino, J.J. Bian, H.S. Shahabi, D. Sopu, J. Sort, J. Eckert, G. Liu, Ductile bulk metallic glass by controlling structural heterogeneities, Sci. Rep. 8 (2018).
[58] S. Scudino, B. Jerliu, S. Pauly, K.B. Surreddi, U. Kühn, J. Eckert, Ductile bulk metallic glasses produced through designed heterogeneities, Scr. Mater. 65 (9) (2011) 815–818.
[59] B.G. Yoo, J.I. Jang, A study on the evolution of subsurface deformation in a Zr-based bulk metallic glass during spherical indentation, J. Phys. D 41 (7) (2008).
[60] S. Scudino, K.B. Surreddi, Shear band morphology and fracture behavior of cold-rolled Zr52.5Ti5Cu18Ni14.5Al10 bulk metallic glass under tensile loading, J. Alloys Compd. 708 (2017) 722–727.
[61] H. Shakur Shahabi, S. Scudino, I. Kaban, M. Stoica, B. Escher, S. Menzel, G. Bm Vaughan, U. Kühn, J. Eckert, Mapping of residual strains around a shear band in bulk metallic glass by nanobeam X-ray diffraction, Acta Mater. 111 (2016) 187–193.
[62] K. Kosiba, D. Sopu, S. Scudino, L. Zhang, J. Bednarcik, S. Pauly, Modulating heterogeneity and plasticity in bulk metallic glasses: role of interfaces on shear banding, Int. J. Plast. 119 (2019) 156–170.
[63] A.L. Greer, Y.Q. Cheng, E. Ma, Shear bands in metallic glasses, Mater. Sci. Eng. R 74 (4) (2013) 71–132.
[64] D. Sopu, A. Stukowski, M. Stoica, S. Scudino, Atomic-level processes of shear band nucleation in metallic glasses, Phys. Rev. Lett. 119 (19) (2017) 195503.
[65] V. Hieronymus-Schmidt, H. Rosner, G. Wilde, A. Zaccone, Shear banding in metallic glasses described by alignments of Eshelby quadrupoles, Phys. Rev. B 95 (13) (2017).